Front. Chem. Sci. Eng. 2023, 17(5): 570−580
https://doi.org/10.1007/s11705-022-2247-y

RESEARCH ARTICLE

Heterometallic cluster-based organic frameworks as highly active electrocatalysts for oxygen reduction and oxygen evolution reaction: a density functional theory study

Xin Chen (✉)[1,2,3], Liang Luo[1], Shihong Huang[1], Xingbo Ge[1], Xiuyun Zhao[4]

1 Center for Computational Chemistry and Molecular Simulation, College of Chemistry and Chemical Engineering, Southwest Petroleum University, Chengdu 610500, China
2 State Key Laboratory of Oil and Gas Reservoir Geology and Exploitation, Southwest Petroleum University, Chengdu 610500, China
3 Oil & Gas Field Applied Chemistry Key Laboratory of Sichuan Province, College of Chemistry and Chemical Engineering, Southwest Petroleum University, Chengdu 610500, China
4 Department of Applied Physics, University of Eastern Finland, Kuopio 70211, Finland

Abstract Recently, metal–organic frameworks are one of the potential catalytic materials for electrocatalytic applications. The oxygen reduction reaction and oxygen evolution reaction catalytic activities of heterometallic cluster-based organic frameworks are investigated using density functional theory. Firstly, the catalytic activities of heterometallic clusters are investigated. Among all heterometallic clusters, Fe_2Mn–Mn has a minimum overpotential of 0.35 V for oxygen reduction reaction, and Fe_2Co–Co possesses the smallest overpotential of 0.32 V for oxygen evolution reaction, respectively 100 and 50 mV lower than those of Pt(111) and RuO_2(110) catalysts. The analysis of the potential gap of Fe_2M clusters indicates that Fe_2Mn, Fe_2Co, and Fe_2Ni clusters possess good bifunctional catalytic activity. Additionally, the catalytic activity of Fe_2Mn and Fe_2Co connected through 3,3′,5,5′-azobenzenetetracarboxylate linker to form Fe_2M–PCN–Fe_2M is explored. Compared with Fe_2Mn–PCN–Fe_2Mn, Fe_2Co–PCN–Fe_2Co, and isolated Fe_2M clusters, the mixed-metal Fe_2Co–PCN–Fe_2Mn possesses excellent bifunctional catalytic activity, and the values of potential gap on the Mn and Co sites of Fe_2Co–PCN–Fe_2Mn are 0.69 and 0.70 V, respectively. Furthermore, the analysis of the electron structure indicates that constructing a mixed-metal cluster can efficiently enhance the electronic properties of the catalyst. In conclusion, the mixed-metal cluster strategy provides a new approach to further design and synthesize high-efficiency bifunctional electrocatalysts.

Keywords bimetallic metal–organic frameworks, bifunctional electrocatalyst, density functional theory, oxygen reduction reaction, oxygen evolution reaction

Received June 15, 2022; accepted August 27, 2022

E-mail: chenxin830107@pku.edu.cn

1 Introduction

The oxygen reduction reaction (ORR) and oxygen evolution reaction (OER) play essential roles in several energy conversion technologies [1–3]. Because of the slow multistep proton-coupled electron transfer process, ORR and OER need efficient electrocatalysts to overcome these kinetic barriers and accelerate the reaction rate [4,5]. Although Pt- and Ru-based catalysts are efficient electrocatalysts for ORR and OER, respectively, their uses are limited due to high costs, natural scarcity, and poor resistance to poisoning [6,7]. Therefore, it becomes very urgent for researchers to develop non-noble metal catalysts for low cost as well as high activity and stability to replace the typical Pt- and Ru-based catalysts.

Recently, more and more non-precious metal materials have been studied, including metal-free carbon-based materials [8,9], metal–nitrogen–carbon materials [10,11], and metal–organic frameworks (MOFs) [12,13]. Among them, MOFs stand out as a type of porous and crystalline materials with structural tunability, high specific surface area, and other beneficial intrinsic physicochemical features [14–17]. Various modification strategies have been investigated, including changing the morphology of MOFs (different organic linkers) [18] or forming heterostructures (bimetallic or multi-metallic MOFs) to develop high-performance MOFs [19–21]. Compared with monometallic materials, bimetallic MOFs materials show more excellent ORR/OER catalytic activity, which

can be attributed to the synergistic effect between different metals [22–24]. For instance, Wang et al. [25] have synthesized a series of stable MOFs based on trinuclear metal carboxylate clusters and tridentate carboxylate ligands (BPTC). The results reveal that the OER catalytic activities of bimetallic Fe_2Co−BPTC, Fe_2Zn−BPTC, and Fe_2Ni-BPTC are improved compared with monometallic Fe_3-BPTC. Additionally, 3,3′,5,5′-azobenzenetetracarboxylate (ABTC), as a type of bridging aromatic tetracarboxylate organic ligand, possesses many advantages to be designed as catalytically-active MOFs [26,27]. For example, the exposed azo bond is from a well-known Lewis base group, which is expected to modulate the catalytic performance. Furthermore, the rigid ABTC ligand has four carboxyl groups, then it is easily deprotonated to form different geometries. In these geometries, several strong metal−oxygen coordination bonds can greatly enhance the thermal stability and rigidity of the framework [28,29]. Recently, Dong et al. [30] have synthesized a series of nanocomposite MOFs materials with porous coordination network structure (Fe_2M−PCN−Fe_2M) composed of the ABTC linker and trinuclear metal cluster, which can construct a mixed-metal-cluster structure with multiple active centers. These findings indicate that Fe_2Ni−PCN−Fe_2Co possesses better OER catalytic activity than Fe_2Ni−PCN−Fe_2Ni and Fe_2Co−PCN−Fe_2Co. Based on these previous studies, it is worthwhile to investigate the potential bifunctional catalytic performance of heterometallic Fe_2M clusters formed using 3d transition metals other than Ni and Co, as well as the effect of mixed heterometallic clusters connected by an ABTC linker on catalytic activity.

This study systematically investigates heterometallic cluster-based organic frameworks' ORR and OER catalytic activities using density functional theory (DFT) methods. First, the structures of heterometallic clusters (Fe_2M, M = Ti, V, Cr, Mn, Co, Ni, Cu, Zn) are constructed. Next, the bifunctional catalytic activity of Fe_2M clusters is investigated, and the Fe_2Mn and Fe_2Co clusters with the most superior catalytic activity are screened. Finally, the Fe_2Mn and Fe_2Co are connected through an ABTC linker to form Fe_2M−PCN−Fe_2M, and the catalytic activity of Fe_2M−PCN−Fe_2M is determined by calculating the binding energy of the reaction intermediate and the Gibbs free energy change of each elementary step.

2 Computational detail

All calculations in this work were employed with a spin-polarized DFT framework and implemented by the DMol^3 module in Materials Studio software [31]. The generalized gradient approximation with the Perdew–Burke–Ernzerhof functional was adopted to describe the electron exchange and correlation effect [32]. The effective core potentials were used to deal with the related relativistic effect, and the basis set of atomic orbitals was described by double numerical polarization. The convergences of energy, maximum force, and maximum displacement were set as 2×10^{-5} Ha, 0.004 Ha·Å^{-1}, and 0.005 Å, respectively.

The stability of the catalyst is evaluated by calculating the substitution energy, which is the energy of M atom replace Ni atom in Fe_2Ni, due to the good stability of synthesized Fe_2Ni cluster according to the experiment [30,33]. The substitution energy (E_{sub}) is calculated as follows:

$$E_{sub} = E_{Fe_2M} + E_{Ni} - E_{Fe_2Ni} - E_M, \quad (1)$$

where E_{Fe_2M}, E_{Ni}, E_{Fe_2Ni}, and E_M are the energies of Fe_2M clusters, isolated Ni atom in bulk phase, Fe_2Ni cluster, and isolated M atom of Fe_2M clusters in bulk phase, respectively. When the calculated value of E_{sub} is negative, it means that the replacement of Ni by other M atoms is energetically favorable, that is, the structure of Fe_2M is more stable than that of Fe_2Ni.

It is well known that ORR has two different reaction pathways, namely two-electron and four-electron pathways. In this paper, only the four-electron pathway with higher power output has been investigated [34,35]. The specific reaction steps of the four-electron pathway are as follows (The asterisk represents the active site of catalysts):

$$* + O_2 + H^+ + e^- \rightarrow *OOH \quad (2)$$

$$*OOH + H^+ + e^- \rightarrow *O + H_2O \quad (3)$$

$$*O + H^+ + e^- \rightarrow *OH \quad (4)$$

$$*OH + H^+ + e^- \rightarrow * + H_2O \quad (5)$$

The binding energies of reaction intermediates ($\Delta E_{species}$) are calculated by the following equations:

$$\Delta E_{*OOH} = E_{*OOH} - E_* - (2E_{H_2O} - 3/2E_{H_2}), \quad (6)$$

$$\Delta E_{*O} = E_{*O} - E_* - (E_{H_2O} - E_{H_2}), \quad (7)$$

$$\Delta E_{*OH} = E_{*OH} - E_* - (E_{H_2O} - 1/2E_{H_2}), \quad (8)$$

where the E_{*OOH}, E_{*O}, and E_{*OH} are the total energies of the catalyst combined with *OOH, *O, and *OH, respectively. The E_* is the energy of the isolated catalyst. The E_{H_2O} and E_{H_2} are the total energies of H_2O and H_2 molecules, respectively.

The Gibbs free energy change is one of the important parameters used to evaluate the catalytic activity of a catalyst, and the specific calculation equations are as follows:

$$\Delta G_1 = \Delta G_{*OOH} - 4.92, \quad (9)$$

$$\Delta G_2 = \Delta G_{*O} - \Delta G_{*OOH}, \quad (10)$$

$$\Delta G_3 = \Delta G_{*\mathrm{OH}} - \Delta G_{*\mathrm{O}}, \quad (11)$$

$$\Delta G_4 = -\Delta G_{*\mathrm{OH}}, \quad (12)$$

where the ΔG_1, ΔG_2, ΔG_3, and ΔG_4 represent the Gibbs free energy change of each step of ORR. The $\Delta G_{*\mathrm{OOH}}$, $\Delta G_{*\mathrm{O}}$, and $\Delta G_{*\mathrm{OH}}$ are the adsorption free energies of *OOH, *O, and *OH, respectively. The adsorption free energies of reaction intermediates ($\Delta G_{*\mathrm{species}}$) are calculated by the equation of $\Delta G_{*\mathrm{species}} = \Delta E_{\mathrm{species}} + \Delta \mathrm{ZPE} - T\Delta S$. Based on the previous work, the zero-point energies and entropies of intermediates adsorbed on different catalysts are similar [36]. Therefore, the $\Delta G_{*\mathrm{species}}$ can be described by $\Delta G_{*\mathrm{OOH}} = \Delta E_{*\mathrm{OOH}} + 0.40$, $\Delta G_{*\mathrm{O}} = \Delta E_{*\mathrm{O}} + 0.05$, and $\Delta G_{*\mathrm{OH}} = \Delta E_{*\mathrm{OH}} + 0.35$. The overpotential of ORR can be calculated by the following equation:

$$\eta^{\mathrm{ORR}} = \max(\Delta G_1, \Delta G_2, \Delta G_3, \Delta G_4)/\mathrm{e} + 1.23. \quad (13)$$

For OER, as is well known that it is the reverse reaction of ORR [37,38]. The Gibbs free energy of each elementary reaction step of OER is the opposite value of the Gibbs free energy of the corresponding ORR step, $\Delta G_{\mathrm{OER}} = -\Delta G_{\mathrm{ORR}}$. The overpotential of OER is calculated by the following equation:

$$\eta^{\mathrm{OER}} = \max(-\Delta G_4, -\Delta G_3, -\Delta G_2, -\Delta G_1)/\mathrm{e} - 1.23. \quad (14)$$

Based on the previous works [39,40], the potential gap (ΔE) is defined to reflect the bifunctional catalytic activity, and the specific equation is as follows:

$$\Delta E = \eta^{\mathrm{ORR}} + \eta^{\mathrm{OER}}. \quad (15)$$

3 Results and discussion

3.1 Structure and catalytic activity of Fe_2M clusters

In this work, the constructed Fe_3 cluster structure, the considered transition metals, and the established Fe_2Ti cluster (which is one of the heterometallic Fe_2M clusters, M = Ti, V, Cr, Mn, Co, Ni, Cu, Zn) are shown in Fig. 1. Firstly, the MIL-88 (Materials of Institute Lavoisier) [41], namely, the Fe_3 cluster, is constructed, as shown in Fig. 1(a). It can be observed that the three Fe sites are joined by a central μ_3-O atom and connected by the carboxylate linkers. Subsequently, a Fe atom in the Fe_3 cluster is replaced with a 3d transition metal atom to examine the catalytic performance of bimetallic MOF catalysts, and the considered transition metals are shown in Fig. 1(b). The optimized configurations of Fe_2M clusters are expressed in Fig. S1 (cf. Electronic Supplementary Material, ESM). It can be clearly observed that all Fe_2M clusters have not undergone deformation compared to Fe_3 cluster. In order to accurately appraise the stability of Fe_2M, the E_{sub} values are calculated and plotted in Table S1 (cf. ESM). It can be found that all E_{sub} values are negative, demonstrating that the substitution of M atom to Ni atom is energetically favorable. Compared with Fe_2Ni, all the Fe_2M being studied possess satisfactory thermodynamical stability. Moreover, the first-principles molecular dynamics calculations are also performed during a period of 1 ps at 300 and 500 K temperatures, respectively. After dynamics calculations, the final structures and the M–O bond lengths of Fe_2M clusters are shown in Fig. S2 (cf. ESM). It is clearly observed that all Fe_2M clusters have no obvious deformation, and the change in bond length is insignificant (no more than 0.15 Å), indicating that they are stable. In each Fe_2M clusters, both the Fe and doped M are considered as active sites. Taking the Fe_2Ti cluster as an example (Fig. 1(c)), Fe_2Ti–Ti and Fe_2Ti–Fe represent the Ti and Fe sites of the Fe_2Ti cluster, respectively. Likewise, naming the active sites of other Fe_2M clusters also follows this rule.

The $\Delta E_{\mathrm{species}}$ on all possible active sites of Fe_2M clusters are calculated to examine the catalytic activity of Fe_2M clusters, as listed in Table 1. For comparison, the values of $\Delta E_{\mathrm{species}}$ on the Pt(111) [42] and RuO_2(110) [43] surfaces are used as a benchmark for ORR and OER, respectively. The smaller the value of $\Delta E_{\mathrm{species}}$, the stronger the binding strength. As is known to us, compared with the ideal ORR catalyst, the Pt(111) surface binds *OOH relatively weak and binds *O and *OH relatively strong. Meanwhile, compared with the ideal OER catalyst, the RuO_2(110) surface binds *O slightly weak. The $\Delta E_{\mathrm{species}}$ values on Fe_2Ti, Fe_2V, and Fe_2Cr clusters are significantly smaller than Pt(111) or RuO_2(110), implying that the binding strength of reaction intermediates on

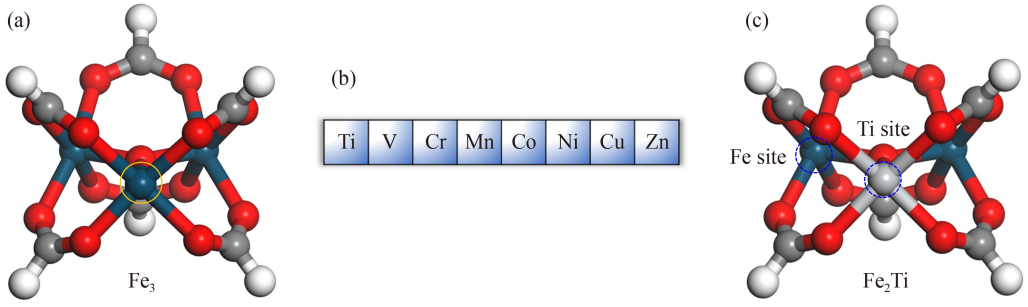

Fig. 1 (a) Optimized configuration of Fe_3 cluster. The orange circle represents the location of the metal to be replaced. (b) Transition metals considered in this work. (c) Active sites of Fe_2Ti cluster. The blue dotted circle represents the active site.

them is excessively strong. In contrast, the values of $\Delta E_{species}$ on Fe_2Cu and Fe_2Zn clusters are significantly larger than that on Pt(111) or RuO_2(110), showing their weak binding strength of reaction intermediates. Therefore, the OER and ORR catalytic activities of the above catalysts may be unsatisfactory. Surprisingly, for Fe_2Mn and Fe_2Co clusters, the $\Delta E_{species}$ values of reaction intermediates are all relatively close to that on the Pt(111) and RuO_2(110) surfaces, proving that they may have excellent ORR and OER activities. It is worth noting that the binding strength of reaction intermediates on the M site of Fe_2M clusters (M = Ti, V, Cr, Mn) is almost stronger than that on the Fe site.

The $\Delta G_{*species}$ values of the reaction intermediates on Fe_2M clusters are calculated and depicted in Fig. 2. It can be detected that there are significant linear relationships of ΔG_{*OOH} and ΔG_{*O} with ΔG_{*OH} on Fe_2M clusters. Generally, *O forms a double bond with the catalyst surface, and *OH forms a single bond with the catalyst surface. The O atom of *OOH forms a single bond with the metal atom. Consequently, the slope between ΔG_{*O} and ΔG_{*OH} is greater than 1, and the slope of ΔG_{*OOH} vs. ΔG_{*OH} is close to 1 [44]. The correlation between ΔG_{*OOH} and ΔG_{*OH} can be explained by $\Delta G_{*OOH} = 0.76\Delta G_{*OH} + 3.27$ with the coefficients of determination (R^2) of 0.88. The slope and intercept are similar to those reported in previous studies [45,46]. Furthermore, the ΔG_{*O} and ΔG_{*OH} display a linear correlation of $\Delta G_{*O} = 1.36\Delta G_{*OH} + 1.29$, and they have a stronger linear relationship due to a higher R^2 value of 0.96. Based on the above analysis, it can be predicted that when Fe_2M clusters have a strong binding ability of *OH, they also interact strongly with *O and *OOH.

Table 1 $\Delta E_{species}$ values of reaction intermediates on all possible active sites of Fe_2M clusters

Active site	ΔE_{*OOH}/eV	ΔE_{*O}/eV	ΔE_{*OH}/eV
Fe_2Ti–Ti	1.66	−0.44	−1.72
Fe_2Ti–Fe	3.20	0.86	−1.01
Fe_2V–V	2.07	−0.48	−1.14
Fe_2V–Fe	3.00	1.60	0.02
Fe_2Cr–Cr	2.22	0.56	−0.85
Fe_2Cr–Fe	2.52	1.33	−0.31
Fe_2Mn–Mn	3.71	2.69	0.70
Fe_2Mn–Fe	4.06	2.67	1.04
Fe_2Co–Co	4.04	2.84	1.02
Fe_2Co–Fe	3.97	3.00	1.00
Fe_2Ni–Ni	3.76	2.80	0.57
Fe_2Ni–Fe	3.20	2.32	0.26
Fe_2Cu–Cu	4.27	4.49	1.93
Fe_2Cu–Fe	4.29	3.28	1.19
Fe_2Zn–Zn	4.38	4.60	1.85
Fe_2Zn–Fe	4.28	3.28	1.19
Pt(111)	3.66	1.65	0.88
RuO_2(110)	3.91	2.66	0.97

According to the linear relationships of ΔG_{*OOH} and ΔG_{*O} with ΔG_{*OH}, ΔG_{*OH} can be determined as the descriptor to explore the catalytic activity of Fe_2M clusters. In addition, by introducing the linear relationships into the Eqs. (8)−(11), the equations can be expressed as $\Delta G_1 = 0.76\Delta G_{*OH} - 1.65$, $\Delta G_2 = 0.60\Delta G_{*OH} - 1.98$, $\Delta G_3 = -0.36\Delta G_{*OH} - 1.29$, and $\Delta G_4 = -\Delta G_{*OH}$. Therefore, the volcano plot between overpotential and ΔG_{*OH} is established, as shown in Fig. 3. In addition, the potential-determining step (PDS) is determined by the step with the maximum ΔG value.

For ORR, the top of the volcano appears (inverted) when ΔG_{*OH} value reaches 0.94 eV, and the minimum theoretical η^{ORR} value of this kind of catalyst is 0.29 V. For Fe_2M clusters with the strong binding strength of *OH (ΔG_{*OH} < 0.94 eV), the *OH reduction step is determined as the PDS. As the ΔG_{*OH} values on Fe_2M clusters increase, the data points fall near the blue line, indicating that the PDS becomes the step of *OOH formation. Additionally, it can be clearly observed that the values of ΔG_{*OH} on Fe_2Mn–Mn and Fe_2Ni–Ni are close to 0.94 eV, manifesting that these catalysts possess

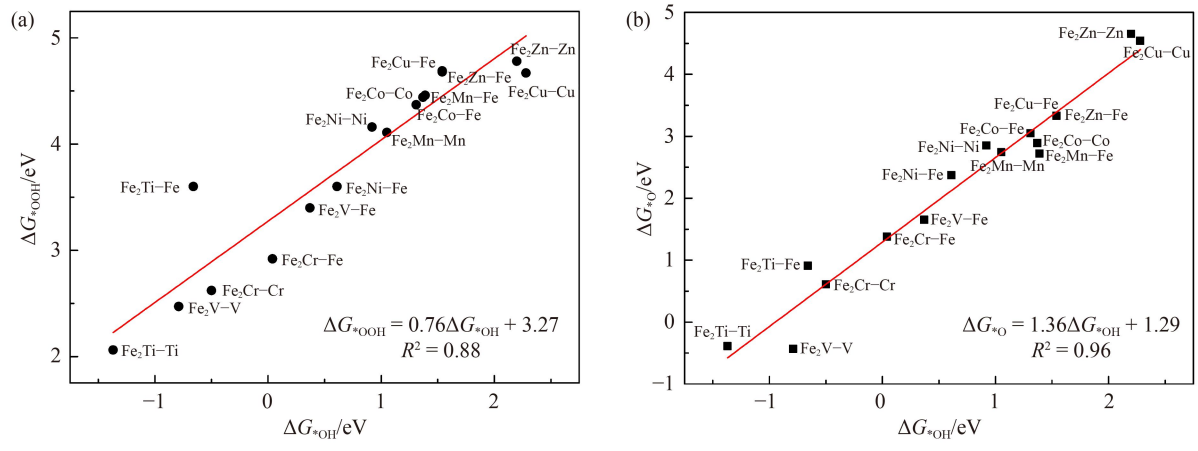

Fig. 2 Scaling relationships of (a) ΔG_{*OOH} vs. ΔG_{*OH} and (b) ΔG_{*O} vs. ΔG_{*OH} on Fe_2M clusters.

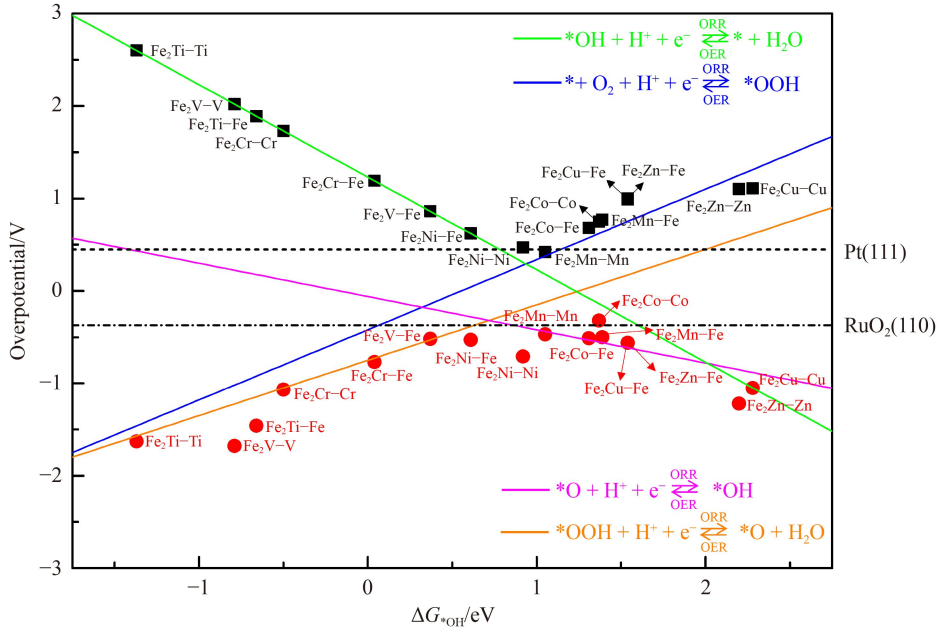

Fig. 3 Volcano plot of η^{ORR} and $-\eta^{OER}$ as a function of ΔG_{*OH} (the square and circle symbols represent η^{ORR} and $-\eta^{OER}$, respectively). Taking ORR as an example, blue line: $\eta^{ORR} = 0.76\Delta G_{*OH} - 0.42$; orange line: $\eta^{ORR} = 0.60\Delta G_{*OH} - 0.75$; purple line: $\eta^{ORR} = -0.36\Delta G_{*OH} - 0.06$; green line: $\eta^{ORR} = -\Delta G_{*OH} + 1.23$.

good catalytic activity. Notably, the η^{ORR} value of Fe_2Mn–Mn is the minimum (0.42 V), which is smaller than the corresponding value of the Pt(111) surface ($\eta^{ORR} = 0.45$ V) [42], showing that the catalytic activity of Fe_2Mn−Mn is comparable to that on the Pt(111) surface.

For OER, the volcanic top appears when ΔG_{*OH} value is equal to 0.72 eV, and the minimum theoretical η^{OER} value is calculated as 0.32 V. When ΔG_{*OH} value is less than 0.72 eV, the PDS of Fe_2M clusters is the third proton-coupled electron transfer step (*O → *OOH). As the binding strength of *OH on Fe_2M clusters weakens, the PDS is calculated as the step of *OH → *O or H_2O → *OH. Apparently, Fe_2Co−Co possesses the smallest η^{OER} value of 0.32 V, which is smaller than the corresponding value on the RuO_2(110) surface (η^{OER} = 0.37 V) [43], manifesting that it has excellent catalytic activity toward OER.

3.2 Bifunctional catalytic activity of Fe_2M clusters

To further examine the bifunctional catalytic activity of this material, the values of ΔE on Fe_2M clusters are calculated and shown in Fig. 4. The smaller the values of ΔE, the better the bifunctional catalytic performance of Fe_2M clusters. Among all Fe_2M clusters, it can be clearly noticed that Fe_2Mn, Fe_2Co, and Fe_2Ni clusters possess better bifunctional catalytic activity due to their smaller ΔE values. Furthermore, the energy gap (E_{gap}) values between the highest occupied molecular orbital (HOMO) and the lowest unoccupied molecular orbital (LUMO) of Fe_2M clusters are calculated to investigate their electronic property, as shown in Table 2. As is well known, a relatively small E_{gap} value implies high chemical reactivity and low dynamic stability [47]. In addition, our previous work has pointed out that an appropriate HOMO value is conducive to the transfer of electrons from the catalyst to O_2, which can weaken the O−O bond and further promote the subsequent reaction process [48]. Compared with other Fe_2M clusters, Fe_2Mn, Fe_2Co, and Fe_2Ni have moderate E_{gap} and HOMO values. This may explain why they possess good bifunctional activity.

3.3 Structure and catalytic activity of Fe_2M–PCN–Fe_2M

Although Fe_2Mn–Mn and Fe_2Co–Co have the highest ORR and OER catalytic activity, respectively, their bifunctional catalytic activities are not ideal. Compared with some reported bifunctional catalysts, including carbon nanotube-supported trimetallic (Mn–Ni–Fe) oxide catalyst (ΔE = 0.73 V) [49], Ni_3Fe nanoparticles embedded in porous nitrogen-doped carbon sheets catalyst (ΔE = 0.84 V) [50], and commercial carbon-supported iridium metal nanoparticles catalyst (ΔE = 0.92 V) [51], the ΔE values of Fe_2Mn and Fe_2Co clusters are relatively larger. To further promote their bifunctional catalytic activity, Fe_2–PCN–Fe_2M is constructed, in which Fe_2Mn and Fe_2Co clusters are connected through the organic linker ABTC. Instead of interacting with the metal element, the carboxylate linker in the heterometallic cluster interacts with the ABTC linker. The optimal configurations of Fe_2Mn–PCN–Fe_2Mn, Fe_2Co–PCN–Fe_2Co, and Fe_2Co–PCN–Fe_2Mn are shown in Fig. 5. Additionally, only Mn and Co sites are considered active sites for the corresponding catalysts due to the fact that

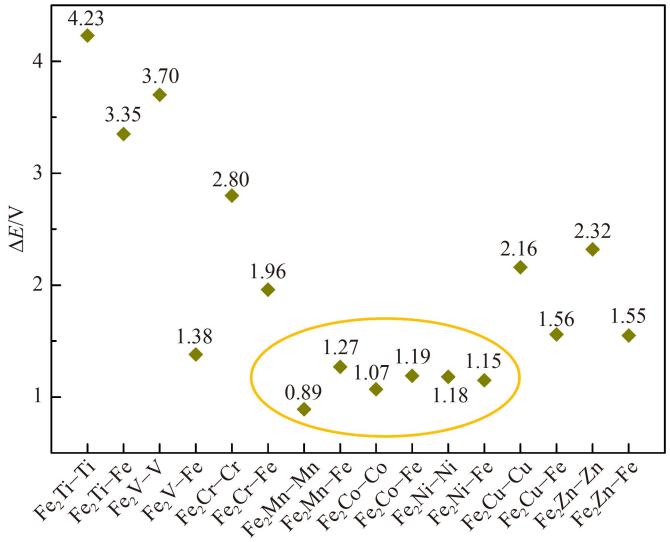

Fig. 4 Values of ΔE on Fe_2M clusters.

Table 2 HOMO, LUMO, and E_{gap} values of Fe_2M clusters

Item	Fe_2Ti	Fe_2V	Fe_2Cr	Fe_2Mn	Fe_2Co	Fe_2Ni	Fe_2Cu	Fe_2Zn
HOMO/eV	−4.749	−4.724	−4.708	−5.859	−5.792	−5.269	−5.985	−6.146
LUMO/eV	−3.829	−4.311	−4.087	−5.049	−4.978	−4.672	−5.041	−4.995
E_{gap}/eV	0.920	0.413	0.621	0.810	0.814	0.597	0.944	1.151

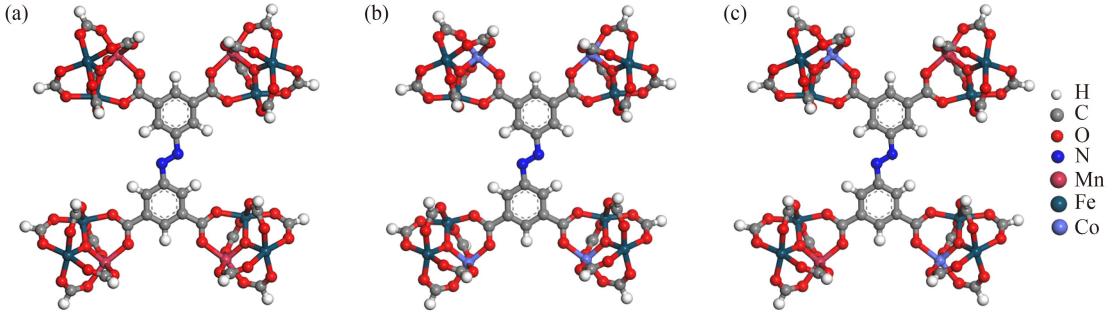

Fig. 5 Optimal configurations of (a) Fe_2Mn–PCN–Fe_2Mn, (b) Fe_2Co–PCN–Fe_2Co, and (c) Fe_2Co–PCN–Fe_2Mn.

Fe_2Mn–Mn and Fe_2Co–Co, respectively, have the best ORR and OER catalytic activity, as well as relatively small ΔE values.

The optimal configurations of the reaction intermediates on Fe_2M–PCN–Fe_2M are calculated, as shown in Fig. S3 (cf. ESM). Meanwhile, the corresponding $\Delta E_{species}$ on Fe_2M–PCN–Fe_2M are calculated, as presented in Table 3. For ORR, the ΔE_{*OOH} values on almost all Fe_2M–PCN–Fe_2M are smaller than those on Fe_2Mn–Mn and Fe_2Co–Co, suggesting the binding strength of *OOH is enhanced on almost all Fe_2M–PCN–Fe_2M. The findings show that the catalytic activities of Fe_2M–PCN–Fe_2M may be improved. Moreover, except for Fe_2Co–PCN–Fe_2Co, the values of ΔE_{*O} and ΔE_{*OH} on Fe_2M–PCN–Fe_2M do not change significantly compared with those on Fe_2Mn–Mn and Fe_2Co–Co. Specifically, Fe_2Co–PCN–Fe_2Co possesses the ΔE_{*O} value of 3.15 eV, which is much larger than the corresponding values on Fe_2Co–Co (2.84 eV) and Pt(111) (1.65 eV), indicating that such weak *O binding strength may cause the ORR process restricted by the formation of *O.

Table 3 $\Delta E_{species}$ values on Fe_2M–PCN–Fe_2M

Catalyst	Site	ΔE_{*OOH}/eV	ΔE_{*O}/eV	ΔE_{*OH}/eV
Fe_2Mn–PCN–Fe_2Mn	Mn site	3.71	2.56	0.61
Fe_2Co–PCN–Fe_2Co	Co site	3.61	3.15	0.82
Fe_2Co–PCN–Fe_2Mn	Mn site	3.68	2.55	0.72
	Co site	3.68	2.82	0.98

For OER, the PDS of Fe_2Mn–Mn and Fe_2Co–Co is the step of *OH → *O, which is attributed to the weak binding strength of *O. Fortunately, the values of ΔE_{*O} on almost all Fe_2M–PCN–Fe_2M are smaller than that on Fe_2Mn–Mn and Fe_2Co–Co, implying stronger *O

binding. Therefore, their OER catalytic activity may be improved by the strong binding strength of *O. As is well known, the ΔE_{*OOH}, ΔE_{*O}, or ΔE_{*OH} alone is insufficient to predicate catalytic activity. Hence, the detailed catalytic process and overpotential are further discussed.

The Gibbs free energy change in each reaction step of ORR and OER on Fe_2M–PCN–Fe_2M is calculated, as shown in Fig. 6. For ORR, it can be found that the free energy curves of each ORR step on all Fe_2M–PCN–Fe_2M being studied are downhill, showing that ORR can occur spontaneously on them. Except for Fe_2Co–PCN–Fe_2Co, the PDS of all Fe_2M–PCN–Fe_2M is the first proton–electron transfer step (the formation of *OOH). The PDS of Fe_2Co–PCN–Fe_2Co is the step of *OOH → *O, which is attributed to its weak binding strength to *O. The corresponding η^{ORR} values on Fe_2Mn–PCN–Fe_2Mn, Fe_2Co–PCN–Fe_2Co, as well as the Mn and Co sites of Fe_2Co–PCN–Fe_2Mn are 0.42, 0.41, 0.39, and 0.39 V, respectively, demonstrating that they have remarkable catalytic activity, even better than the Pt(111) surface (η^{ORR} = 0.45 V) [42]. For OER, the PDS of all Fe_2M–PCN–Fe_2M being studied is the step of *OH → *O. It is noteworthy that the Mn and Co sites of Fe_2Co–PCN–Fe_2Mn have small η^{OER} values of 0.30 and 0.31 V, respectively. These values are even less than that on the RuO_2(110) surface (0.37 V) [43], indicating that Fe_2Co–PCN–Fe_2Mn possesses excellent OER catalytic activity. Furthermore, some experimental studies have shown that the Fe_2Co cluster-based organic frameworks exhibit excellent OER performance, including Fe_2Co–MOF (0.34 V) [17] and Fe_2Co-BPTC (0.38 V) [25].

Additionally, the bifunctional catalytic activity of Fe_2M–PCN–Fe_2M is also investigated. For Fe_2Co–PCN–Fe_2Co, its ΔE value (1.17 V) is larger than that for Fe_2Co–Co (1.07 V), implying its inferior bifunctional catalytic activity. For Fe_2Mn–PCN–Fe_2Mn, its ΔE value only becomes 0.05 V smaller than Fe_2Mn–Mn (0.89 to 0.84 V). Following the above analysis, forming Fe_2M–PCN–Fe_2M by the same Fe_2M clusters cannot significantly improve the bifunctional catalytic activity. Encouragingly, when forming mixed-metal Fe_2Co–PCN–Fe_2Mn, the ΔE values on the Mn and Co sites on it are 0.69 and 0.70 V, respectively, significantly smaller than the corresponding values on Fe_2Co–Co, Fe_2Mn–Mn, and other previously reported catalysts [49–51]. All in all, forming mixed-metal Fe_2Co–PCN–Fe_2Mn is an effective strategy to improve the bifunctional catalytic performance of the original Fe_2M clusters.

3.4 Origin of the activity

The number of electrons in the 3d orbital of Mn or Co

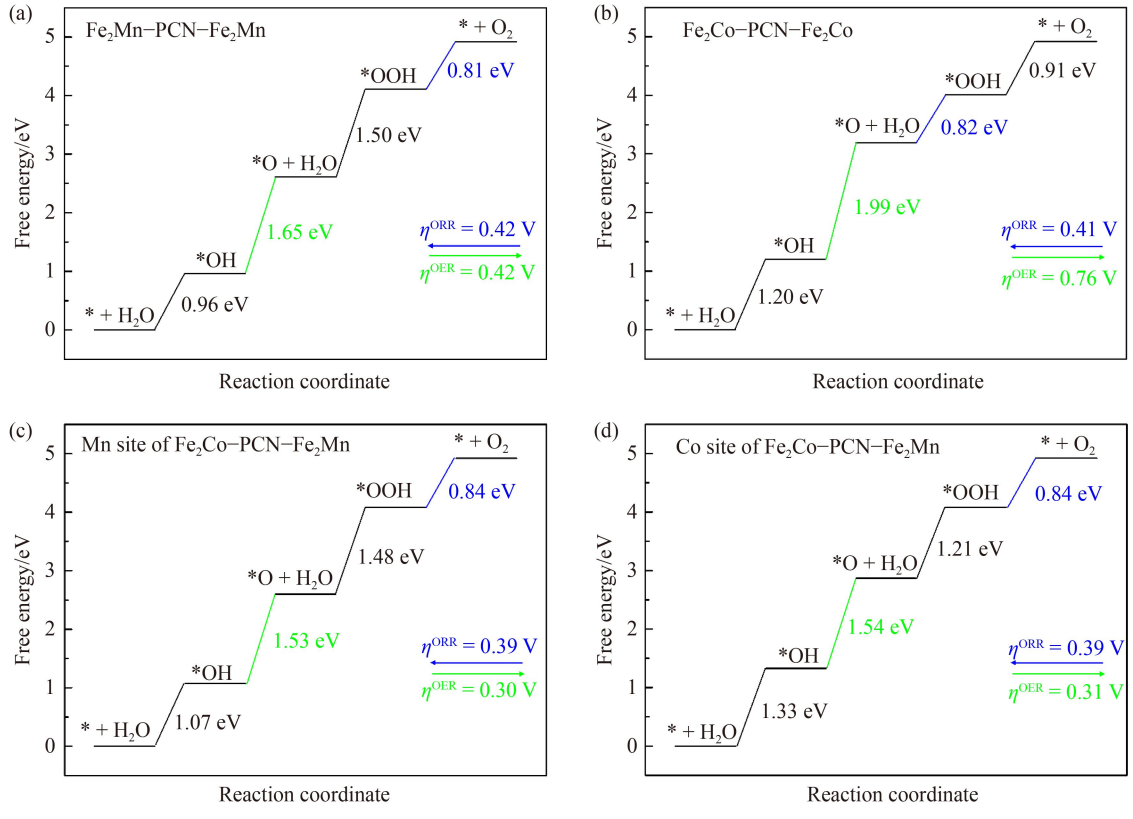

Fig. 6 Free energy diagrams of ORR and OER on (a) Fe_2Mn–PCN–Fe_2Mn, (b) Fe_2Co–PCN–Fe_2Co, (c) Mn site of Fe_2Co–PCN–Fe_2Mn, and (d) Co site of Fe_2Co–PCN–Fe_2Mn. The PDS of ORR and OER are denoted by blue and green lines, respectively.

active atoms of Fe_2Co–PCN–Fe_2Mn, Fe_2Co, and Fe_2Mn is calculated to investigate the origin of catalytic activity of Fe_2Co–PCN–Fe_2Mn. A previous study has found that a greater number of electrons in the 3d orbital of an active metal atom is more conducive to the binding of *OOH [52]. As shown in Fig. 7, the profiles of density of states (DOS) are integrated to calculate the accurate number of electrons in 3d orbital metal atom. The number of electrons under the Fermi level in 3d orbitals of the Mn and Co sites of Fe_2Co–PCN–Fe_2Mn is 8.75e and 10.72e, which are respectively larger than that of the Mn site of Fe_2Mn (8.44e) and Co site of Fe_2Co (9.59e). The greater number of electrons in the 3d orbital makes the Mn and Co sites of Fe_2Co–PCN–Fe_2Mn have stronger *OOH binding strength than that on the Mn site of Fe_2Mn and Co site of Fe_2Co, respectively, which is proven by the calculated values of ΔE_{*OOH} (Table 1 and 3). Additionally, taking Fe_2Mn and Fe_2Co–PCN–Fe_2Mn as examples, the corresponding DOS is calculated to reflect the electronic properties of catalysts before and after forming a mixed-metal cluster, as shown in Fig. 8. It can be observed that the Mn-d orbitals of the catalysts overlap with O-p orbitals of *OOH near the Fermi level, implying that the specific interaction between the catalyst and *OOH. Compared with the case of Fe_2Mn, the peak of O-p orbitals of *OOH on Fe_2Co–PCN–Fe_2Mn is split into several peaks and shifted to a lower energy level, indicating the stronger orbital hybridization between Mn-d and O-p orbitals. Therefore, the results reveal that the strategy of constructing a mixed-metal cluster can effectively tune the electronic property of the active site, increasing the catalytic activity of the catalyst.

4 Conclusions

The ORR and OER catalytic activities of heterometallic cluster-based organic frameworks are systematically explored by DFT methods in this work. Firstly, the

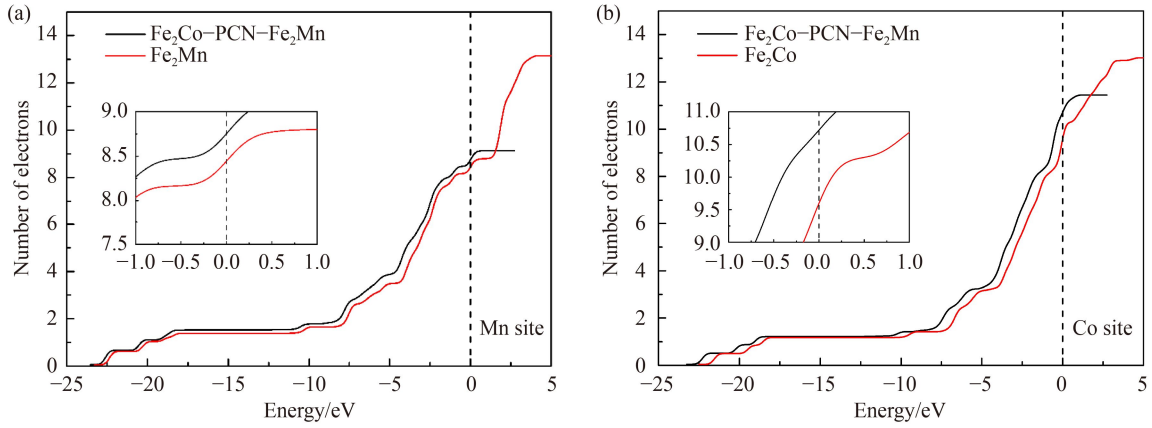

Fig. 7 (a) The number of electrons in the 3d orbital of Mn active atoms of Fe_2Co–PCN–Fe_2Mn and Fe_2Mn; (b) the number of electrons in the 3d orbital of Co active atoms of Fe_2Co–PCN–Fe_2Mn and Fe_2Co. The Fermi level is set to zero. Inset is the magnified pattern near the Fermi level.

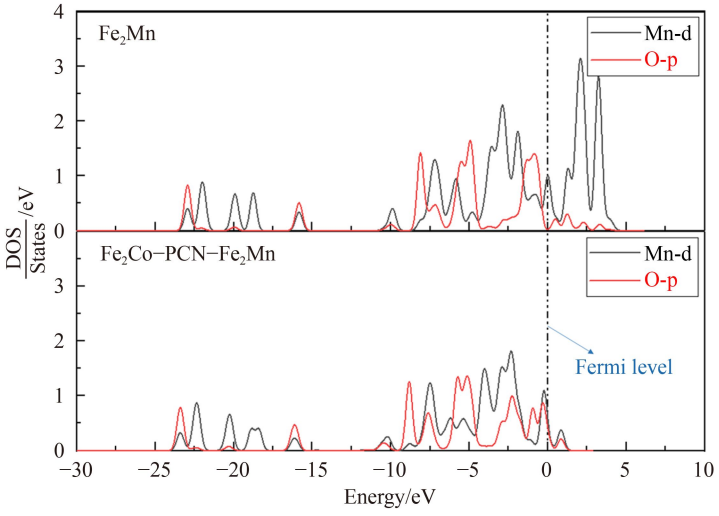

Fig. 8 DOS of d orbitals for Fe_2Mn and Fe_2Co–PCN–Fe_2Mn. The O-p refers to the p orbital of the oxygen atom of *OOH.

binding strength of the reaction intermediates on Fe_2M clusters is studied. It can be found that Fe_2Mn and Fe_2Co clusters may have excellent ORR and OER catalytic activities due to the $\Delta E_{species}$ values on them are close to that on the Pt(111) and RuO_2(110) surfaces. Subsequently, the scaling relationships of ΔG_{*OOH} and ΔG_{*O} with ΔG_{*OH} on Fe_2M clusters are established, and the volcano plot between the overpotential and ΔG_{*OH} is constructed. Fe_2Mn–Mn possesses the highest ORR activity (η^{ORR} = 0.42 V), which is better than the Pt(111) surface (η^{ORR} = 0.45 V). Fe_2Co−Co has the smallest η^{OER} value of 0.32 V, which is smaller than that on the RuO_2(110) surface (η^{OER} = 0.37 V). Additionally, the potential gap on Fe_2M clusters is calculated to assess the bifunctional catalytic activity. Among them, Fe_2Mn, Fe_2Co, and Fe_2Ni clusters have better bifunctional catalytic activity due to the ΔE values on them being relatively small. Furthermore, Fe_2M–PCN–Fe_2M formed by Fe_2Mn and Fe_2Co clusters is constructed, and the bifunctional catalytic activity is investigated. For ORR, except for Fe_2Co–PCN–Fe_2Co (*OOH → *O), the PDS of all Fe_2M–PCN–Fe_2M is the formation of *OOH. Compared with the Pt(111) surface, the η^{ORR} values on all Fe_2M–PCN–Fe_2M being studied are smaller, indicating that they have excellent ORR catalytic activity. For OER, the PDS of all Fe_2M–PCN–Fe_2M under study is the step of *OH → *O. Fe_2Co–PCN–Fe_2Mn possesses excellent OER catalytic activity due to the small η^{OER} values on the Mn and Co sites of the catalyst. Encouragingly, it can be found that both the Mn and Co sites of Fe_2Co–PCN–Fe_2Mn have excellent bifunctional catalytic activity, which is attributed to their potential gap of 0.69 and 0.70 V, respectively. Moreover, the analysis of the number of electrons in the 3d orbital of an active metal atom indicates that formed mixed-metal Fe_2Co–PCN–Fe_2Mn can effectively tune the electronic properties of the active site. These results demonstrate that mixing Fe_2Co and Fe_2Mn clusters to construct mixed-metal Fe_2Co–PCN–Fe_2Mn is an effective strategy to improve the catalytic activity of the original Fe_2M clusters.

Acknowledgements This work was supported by the Science and Technology Project of Sichuan Province (Grant No. 2022YFS0447), the Local Science and Technology Development Fund Projects Guided by the Central Government of China (Grant No. 2021ZYD0060), the Science and Technology Project of Southwest Petroleum University (Grant No. 2021JBGS03), the Special Project of Science and Technology Strategic Cooperation between Nanchong City and Southwest Petroleum University (Grant No. SXQHJH064), and the Postgraduate Research and Innovation Fund of Southwest Petroleum University (Grant No. 2021CXYB14). We acknowledge the National Supercomputing Center in Shenzhen for providing the computational resources and Materials Studio.

Electronic Supplementary Material Supplementary material is available in the online version of this article at https://dx.doi.org/10.1007/s11705-022-2247-y and is accessible for authorized users.

References

1. Li N, Nam Y, Lee J Y. Catalytic nature of iron–nitrogen–graphene heterogeneous catalysts for oxygen evolution reaction and oxygen reduction reaction. Applied Surface Science, 2020, 514: 146073
2. Zheng X, Cao X, Sun Z, Zeng K, Yan J, Strasser P, Chen X, Sun S, Yang R. Indiscrete metal/metal–N–C synergic active sites for efficient and durable oxygen electrocatalysis toward advanced Zn–air batteries. Applied Catalysis B: Environmental, 2020, 272: 118967
3. Deng L, Yang Z, Li R, Chen B, Jia Q, Zhu Y, Xia Y. Graphene-reinforced metal–organic frameworks derived cobalt sulfide/carbon nanocomposites as efficient multifunctional electrocatalysts. Frontiers of Chemical Science and Engineering, 2021, 15(6): 1487–1499
4. Koper M T M. Theory of multiple proton−electron transfer reactions and its implications for electrocatalysis. Chemical Science, 2013, 4(7): 2710–2723
5. Sun F, Li C, Li B, Lin Y. Amorphous MoS: X developed on $Co(OH)_2$ nanosheets generating efficient oxygen evolution catalysts. Journal of Materials Chemistry A: Materials for Energy and Sustainability, 2017, 5(44): 23103–23114
6. Chen X. Oxygen reduction reaction on cobalt-(*n*)pyrrole clusters from DFT studies. RSC Advances, 2016, 6(7): 5535–5540
7. Zhang S, Lv F, Zhang X, Zhang Y, Zhu H, Xing H, Mu Z, Li J, Guo S, Wang E. Ni@RuM (M = Ni or Co) core@shell nanocrystals with high mass activity for overall water-splitting catalysis. Science China Materials, 2019, 62(12): 1868–1876
8. Lu X, Ge L, Yang P, Levin O, Kondratiev V, Qu Z, Liu L, Zhang J, An M. N-doped carbon nanosheets with ultra-high specific surface area for boosting oxygen reduction reaction in Zn−air batteries. Applied Surface Science, 2021, 562: 150114
9. Yu X H, Yi J L, Zhang R L, Wang F Y, Liu L. Hollow carbon spheres and their noble metal-free hybrids in catalysis. Frontiers of Chemical Science and Engineering, 2021, 15(6): 1380–1407
10. Sun C, Li Z, Yang J, Wang S, Zhong X, Wang L. Two-dimensional closely packed amide polyphthalocyanine iron absorbed on Vulcan XC-72 as an efficient electrocatalyst for oxygen reduction reaction. Catalysis Today, 2020, 353: 279–286
11. Zhang Y, Chen X, Zhang H, Ge X. Screening of catalytic oxygen reduction reaction activity of 2, 9-dihalo-1, 10-phenanthroline metal complexes: The role of transition metals and halogen substitution. Journal of Colloid and Interface Science, 2022, 609: 130–138
12. Chen X, Sun F, Bai F, Xie Z. DFT study of the two dimensional metal–organic frameworks $X_3(HITP)_2$ as the cathode electrocatalysts for fuel cell. Applied Surface Science, 2019, 471: 256–262
13. Zhang H, Zhao W, Wu Y, Wang Y, Zou M, Cao A. Dense monolithic MOF and carbon nanotube hybrid with enhanced volumetric and areal capacities for lithium–sulfur battery. Journal of Materials Chemistry A: Materials for Energy and Sustainability, 2019, 7(15): 9195–9201
14. Witman M, Ling S, Anderson S, Tong L, Stylianou K C, Slater B,

Smit B, Haranczyk M. *In silico* design and screening of hypothetical MOF-74 analogs and their experimental synthesis. Chemical Science, 2016, 7(9): 6263–6272

15. Ban Y, Zhao M, Yang W. Metal–organic framework-based CO_2 capture: from precise material design to high-efficiency membranes. Frontiers of Chemical Science and Engineering, 2020, 14(2): 188–215
16. Zhang Z, Chen Y, Wang Z, Hu C, Ma D, Chen W, Ao T. Effective and structure-controlled adsorption of tetracycline hydrochloride from aqueous solution by using Fe-based metal–organic frameworks. Applied Surface Science, 2021, 542: 148662
17. Gu M, Wang S C, Chen C, Xiong D, Yi F Y. Iron-based metal–organic framework system as an efficient bifunctional electrocatalyst for oxygen evolution and hydrogen evolution reactions. Inorganic Chemistry, 2020, 59(9): 6078–6086
18. Shao Q, Yang J, Huang X. The design of water oxidation electrocatalysts from nanoscale metal–organic frameworks. Chemistry, 2018, 24(27): 15143–15155
19. Gao Z, Yu Z W, Liu F Q, Yang C, Yuan Y H, Yu Y, Luo F. Stable iron hydroxide nanosheets@cobalt-metal−organic-framework heterostructure for efficient electrocatalytic oxygen evolution. ChemSusChem, 2019, 12(20): 4623–4628
20. Kirchon A, Zhang P, Li J, Joseph E A, Chen W, Zhou H C. Effect of isomorphic metal substitution on the fenton and photo-fenton degradation of methylene blue using Fe-based metal–organic frameworks. ACS Applied Materials & Interfaces, 2020, 12(8): 9292–9299
21. Gopalsamy K, Babarao R. Heterometallic metal organic frameworks for air separation: a computational study. Industrial & Engineering Chemistry Research, 2020, 59(35): 15718–15731
22. Li S, Gao Y, Li N, Ge L, Bu X, Feng P. Transition metal-based bimetallic MOFs and MOF-derived catalysts for electrochemical oxygen evolution reaction. Energy & Environmental Science, 2021, 14(4): 1897–1927
23. Senthil Raja D, Lin H W, Lu S Y. Synergistically well-mixed MOFs grown on nickel foam as highly efficient durable bifunctional electrocatalysts for overall water splitting at high current densities. Nano Energy, 2019, 57: 1–13
24. Zhou W, Huang D D, Wu Y P, Zhao J, Wu T, Zhang J, Li D S, Sun C, Feng P, Bu X. Stable hierarchical bimetal−organic nanostructures as high performance electrocatalysts for the oxygen evolution reaction. Angewandte Chemie International Edition, 2019, 58(13): 4227–4231
25. Wang X L, Dong L Z, Qiao M, Tang Y J, Liu J, Li Y, Li S L, Su J X, Lan Y Q. Exploring the performance improvement of the oxygen evolution reaction in a stable bimetal–organic framework system. Angewandte Chemie International Edition, 2018, 57(31): 9660–9664
26. Liu W, Ye L, Liu X, Yuan L, Jiang J, Yan C. Hydrothermal syntheses, structures and luminescent properties of d^{10} metal–organic frameworks based on rigid 3,3′,5,5′-azobenzenetetracarboxylic acid. CrystEngComm, 2008, 10(10): 1395–1403
27. Li Y P, Zhang L J, Ji W J. Synthesis, characterization, crystal structure of magnesium compound based 3,3′,5,5′-azobenzentetracarboxylic acid and application as high-performance heterogeneous catalyst for cyanosilylation. Journal of Molecular Structure, 2017, 1133: 607–614
28. Osta R E, Frigoli M, Marrot J, Guillou N, Chevreau H, Walton R I, Millange F. A lithiumeorganic framework with coordinatively unsaturated metal sites that reversibly binds water. Chemical Communications, 2012, 48(86): 10639–10641
29. Saha D, Maity T, Koner S. A magnesium-based multifunctional metal–organic framework: synthesis, thermally induced structural variation, selective gas adsorption, photoluminescence and heterogeneous catalytic study. Dalton Transactions, 2013, 42(38): 13912–13922
30. Dong H, Zhang X, Yan X C, Wang Y X, Sun X, Zhang G, Feng Y, Zhang F M. Mixed-metal-cluster strategy for boosting electrocatalytic oxygen evolution reaction of robust metal–organic frameworks. ACS Applied Materials & Interfaces, 2019, 11(48): 45080–45086
31. Delley B. From molecules to solids with the $DMol^3$ approach. Journal of Chemical Physics, 2000, 113(18): 7756–7764
32. Perdew J P, Burke K, Ernzerhof M. Generalized gradient approximation made simple. Physical Review Letters, 1996, 77(18): 3865–3868
33. Dong L Z, Zhang L, Liu J, Huang Q, Lu M, Ji W X, Lan Y Q. Stable heterometallic cluster-based organic framework catalysts for artificial photosynthesis. Angewandte Chemie International Edition, 2020, 59(7): 2659–2663
34. Chen X, Ge F, Chang J, Lai N. Exploring the catalytic activity of metal-fullerene $C_{58}M$ (M = Mn, Fe, Co, Ni, and Cu) toward oxygen reduction and CO oxidation by density functional theory. International Journal of Energy Research, 2019, 43(13): 7375–7383
35. Modak B, Srinivasu K, Ghosh S K. Exploring metal decorated porphyrin-like porous fullerene as catalyst for oxygen reduction reaction: a DFT study. International Journal of Hydrogen Energy, 2017, 42(4): 2278–2287
36. Calle-Vallejo F, Martínez J I, Rossmeisl J. Density functional studies of functionalized graphitic materials with late transition metals for oxygen reduction reactions. Physical Chemistry Chemical Physics, 2011, 13(34): 15639–15643
37. Chen X, Zhang H, Li X. Mechanisms of fullerene and single-walled carbon nanotube composite as the metal-free multifunctional electrocatalyst for the oxygen reduction, oxygen evolution, and hydrogen evolution. Molecular Catalysis, 2021, 502: 111383
38. Zhao X, Liu X, Huang B, Wang P, Pei Y. Hydroxyl group modification improves the electrocatalytic ORR and OER activity of graphene supported single and bi-metal atomic catalysts (Ni, Co, and Fe). Journal of Materials Chemistry A: Materials for Energy and Sustainability, 2019, 7(42): 24583–24593
39. Ma Y, Jin F, Hu Y H. Bifunctional electrocatalysts for oxygen reduction and oxygen evolution: a theoretical study on 2D metallic WO_2-supported single atom (Fe, Co, or Ni) catalysts. Physical Chemistry Chemical Physics, 2021, 23(24): 13687–13695
40. Wei B, Fu Z, Legut D, Germann T C, Du S, Zhang H, Francisco J S, Zhang R. Rational design of highly stable and active MXene-

based bifunctional ORR/OER double-atom catalysts. Advanced Materials, 2021, 33(40): 2102595

41. Surblé S, Serre C, Mellot-Draznieks C, Millange F, Férey G. A new isoreticular class of metal–organic-frameworks with the MIL-88 topology. Chemical Communications, 2006(3): 284–286
42. Chen X, Sun F, Chang J. Cobalt or nickel doped SiC nanocages as efficient electrocatalyst for oxygen reduction reaction: a computational prediction. Journal of the Electrochemical Society, 2017, 164(6): F616–F619
43. Rossmeisl J, Qu Z W, Zhu H, Kroes G J, Nørskov J K. Electrolysis of water on oxide surfaces. Journal of Electroanalytical Chemistry, 2007, 607(1-2): 83–89
44. Kulkarni A, Siahrostami S, Patel A, Nørskov J K. Understanding catalytic activity trends in the oxygen reduction reaction. Chemical Reviews, 2018, 118(5): 2302–2312
45. He T, Matta S K, Will G, Du A. Transition-metal single atoms anchored on graphdiyne as high-efficiency electrocatalysts for water splitting and oxygen reduction. Small Methods, 2019, 3(9): 1800419
46. Chen X, Huang S, Zhang H. Bimetallic alloys encapsulated in fullerenes as efficient oxygen reduction or oxygen evolution reaction catalysts: a density functional theory study. Journal of Alloys and Compounds, 2022, 894: 162508
47. Aihara J I. Reduced HOMO-LUMO gap as an index of kinetic stability for polycyclic aromatic hydrocarbons. Journal of Physical Chemistry A, 1999, 103(37): 7487–7495
48. Ge F, Qiao Q, Chen X, Wu Y. Probing the catalytic activity of M-$N_{4-x}O_x$ embedded graphene for the oxygen reduction reaction by density functional theory. Frontiers of Chemical Science and Engineering, 2020, 15(5): 1206–1216
49. Morales D M, Kazakova M A, Dieckhöfer S, Selyutin A G, Golubtsov G V, Schuhmann W, Masa J. Trimetallic Mn−Fe−Ni oxide nanoparticles supported on multi-walled carbon nanotubes as high-performance bifunctional ORR/OER electrocatalyst in alkaline media. Advanced Functional Materials, 2020, 30(6): 1905992
50. Fu G, Cui Z, Chen Y, Li Y, Tang Y, Goodenough J B. Ni_3Fe-N doped carbon sheets as a bifunctional electrocatalyst for air cathodes. Advanced Energy Materials, 2017, 7(1): 1601172
51. Gorlin Y, Jaramillo T F. A bifunctional nonprecious metal catalyst for oxygen reduction and water oxidation. Journal of the American Chemical Society, 2010, 132(39): 13612–13614
52. Tang T, Jiang W J, Niu S, Liu N, Luo H, Chen Y Y, Jin S F, Gao F, Wan L J, Hu J S. Electronic and morphological dual modulation of cobalt carbonate hydroxides by Mn doping toward highly efficient and stable bifunctional electrocatalysts for overall water splitting. Journal of the American Chemical Society, 2017, 139(24): 8320–8328